International Communications in Heat and Mass Transfer 159 (2024) 107992

Contents lists available at ScienceDirect

International Communications in Heat and Mass Transfer

journal homepage: www.elsevier.com/locate/ichmt

A shell-tube latent heat thermal energy storage: Influence of metal foam inserts in both shell and tube sides

Aeshah Alasmari [a], Hakim S. Sultan Aljibori [b], Fathi Alimi [c], Mohamed Bouzidi [d,e], Mohammad S. Islam [f], Shima Yazdani [g], Mohammad Ghalambaz [h,g,*]

[a] *Department of Physics, College of Science, University of Bisha, Bisha 61922, Saudi Arabia*
[b] *College of Engineering, University of Warith Al-Anbiyaa, 56001, Karbala, Iraq*
[c] *Department of Chemistry, College of Science, University of Ha'il, P.O. Box 2440, Ha'il 81441, Saudi Arabia*
[d] *Department of Physics, College of Science, University of Ha'il, P.O. Box 2440, Ha'il, Saudi Arabia*
[e] *Laboratoire de Recherche sur les Hétéro-Epitaxies et Applications, Faculty of Science of Monastir, University of Monastir, Monastir 5019, Tunisia*
[f] *School of Mechanical and Mechatronic Engineering, University of Technology Sydney (UTS), 15 Broadway, Ultimo, NSW 2007, Australia*
[g] *Laboratory on Convective Heat and Mass Transfer, Tomsk State University, 634050 Tomsk, Russia*
[h] *Department of Mathematics, Saveetha School of Engineering, SIMATS, Chennai, India*

ARTICLE INFO

Keywords:
Phase change heat transfer
Heat transfer enhancement
Partial layer metal foam
Metal foam insert
Foam layer shape

ABSTRACT

Enhancing heat transfer in latent heat thermal energy storage systems is of utmost importance to facilitate the efficient absorption and release of thermal energy. The primary objective of the current study is to investigate the influence of a metal foam layer on heat transfer enhancement in both the heat transfer fluid side and the shell side. The research explores the incorporation of a fixed 30 % foam layer, which can either extend along the tube wall or penetrate deeper into the shell, moving away from the heat transfer fluid tube. A local thermal non-equilibrium two-temperature heat equation model is utilized to mathematically model the interactions within the metal foam embedded in the heat transfer fluid tube and the phase change material domain. The governing equations are solved using the finite element method. The results indicate that adjustments to the inlet pressure and the metal foam shape parameter (FL) can significantly reduce the melting time, with a variation of approximately 40 %. Specifically, at a constant inlet pressure of 750 Pa, the energy storage power at a 90 % charging increases from 32.2 W (FL = 0.75) to 48.7 W (FL = 1.37). A modification of FL shape parameter increased the power output by 34 %.

1. Introduction

Despite the considerable advantages of solar energy - its inexhaustibility, widespread distribution, and environmental cleanliness - it also presents inherent challenges. A significant issue is its unpredictability, as illumination intensity varies over time [1]. The duration of effective sunlight is confined to just a few hours each day, and its availability is intermittent, displaying inconsistency in both time and space [2]. Consequently, the nature of solar energy prohibits it from providing a constant and unyielding heat source. This underlines the crucial need for incorporating a reliable and high-performing thermal energy storage system to harness this abundant yet capricious resource effectively [3,4].

As of today, there are several key varieties of thermal energy storage, such as thermochemical thermal energy storage [5], latent heat thermal energy storage (LHTES) [6], and sensible heat thermal energy storage [7]. Notably, the energy density of LHTES outperforms the sensible ones by a factor of 5 to 10 [3,8], and it also trumps thermochemical thermal energy storage in safety and reliability. The unique attribute of LHTES is that it maintains a nearly consistent temperature during phase transitions, enabling stable energy charge and discharge. Thus, LHTES finds extensive applications in harnessing solar energy at moderate and low temperatures. For instance, researchers in [9] enhanced the functionality of a solar water heater by incorporating three types of benzene formic acids and erythritol into the vacuum tube collector, achieving a thermal efficiency boost of 26 % and 66 % in normal and charging operations, respectively. The thermal management strategies are a critical aspect of optimizing LHTES performance. Effective thermal management is essential to ensure uniform temperature distribution and prevent

---

* Corresponding author.
E-mail addresses: aymalasmari@ub.edu.sa (A. Alasmari), hakim.s@uowa.edu.iq (H.S.S. Aljibori), MohammadSaidul.Islam@uts.edu.au (M.S. Islam), m.ghalambaz@gmail.com (M. Ghalambaz).

https://doi.org/10.1016/j.icheatmasstransfer.2024.107992

Nomenclature

Latin

A_{mush}	mushy constant value, 10^{10} kg/(m^{3}s)
A_{sf}	interface surface between MF pore and HTF 1/m
C_F	Frochheimer coefficient m
C_p	heat capacity per unit of mass J/(kg.K)
d_{fp}	pore diameter m
d_{fs}	pore characteristics m
dV	volume element m
e	porous structure constant, 0.339
ES	stored energy J
E_s	mushy source term constant value, 0.001
ES_{latent}	stored energy in the latent form J
$ES_{sensible}$	stored energy in sensible form J
FL	MFL shape parameter
g	gravity acceleration m/s^2
H	height m
h_{sf}	interface heat transfer W/(m.K)
h_v	volumetric interface heat transfer W/(m^3.K)
k	thermal conductivity W/(m.K)
L	enclosure width m
Lf	latent heat of fusion J/kg
m	mesh control parameter
M_A, M_B, M_C, M_D	dummy parameters (m.K)/W
MVF	melt fraction
Nu_v	Nusselt number
P_0	outlet pressure Pa
Pi	inlet pressure Pa
Pr	Prandtl number
q	heat rate
r, z	coordinate system m
Re	Reynolds number
RRV_{MF}	HTF metal foam fill ratio
S_{MF}	distance between MF inserts in HTF m
SP	energy storage power W
t	time s
T	temperature field K
T_0	reference temperature K
Tc	cold temperature K
T_f	fusion temperature K
Th	hot temperature K
Tin	inlet temperature K
t_{MF}	MFL thickness m
u	r-velocity component m/s
V	volume m^3
VFL	fill ratio parameter
w	z- velocity component m/s

Greek

α	thermal diffusivity m^2/s
β	volume expansion 1/K
ε	porosity
κ	porous permeability m^2
κ_{tor}	pore flow tortuosity
μ	dynamic viscosity Pa.s
μ_∞	artificial dynamic viscosity, 10^5 Pa.s
ρ	density kg/m^3
σ	dummy parameter
φ	liquid amount
ω	pore per inch (PPI)

Abbreviations

eff	effective property
FL	height ratio parameter
HTF	heat transfer fluid
LHTES	latent heat thermal energy storage
LTNE	local thermal non-equilibrium
MF	metal foam
MFL	metal foam layer in the PCM domain
PCM	phase change material

hotspots, which can significantly affect the system's efficiency and longevity. For instance, research on large-scale high-capacity lithium-ion energy storage systems has demonstrated the effectiveness of forced cooling techniques in controlling temperature variations. A study by Ye and Arıcı [10] revealed that by optimizing airflow channel widths and air gaps between battery modules in a seven-level module configuration, the maximum temperature rise could be limited to 4.63 K, with a temperature uniformity of 2.82 K, thereby maintaining the system within the ideal operating temperature range of less than 313.15 K. Such advancements in thermal management are crucial for enhancing the performance of LHTES systems, as they help to manage the heat generated during phase transitions more effectively, ensuring reliable and efficient energy storage.

A typical LHTES system comprises three main components. The first one is a phase change material (PCM) chosen for its suitable phase transition temperature. The second component is a heat transfer fluid (HTF) with good thermal conductivity. The final element is a container or chamber that houses both the PCM and the HTF.

The shell-and-tube structure for thermal energy storage holds substantial promise for improving efficiency in the field of LHTES systems. However, these systems encounter challenges tied to outlet threshold temperatures, reducing the effective usage of PCM. Thus, a major research goal is to enhance shell-and-tube LHTES performance within these constraints during the charging and discharging phases [11]. Accurate modeling of the phase change process is critical to achieving these enhancements. Recent studies, such as the work by Ye and Arıcı [12], have addressed the need for refined interface error definitions and robust validation methods in phase change modeling, particularly for materials like pure gallium, which shares similar phase transition challenges with common PCMs. Ye and Arıcı [13], have emphasized the importance of 3D validation and the feasibility of 2D modeling in phase change simulations, particularly for materials like pure gallium. They also corrected and developed new correlations for calculating the mean liquid layer thickness and the Nusselt number, which are vital for predicting heat transfer performance in phase change processes. These advancements in numerical techniques ensure that structural modifications, like undulated PCM container shapes and optimized tube arrangements, can be effectively translated into improved performance metrics. Research efforts in [14] reveal that undulated PCM container shapes such as zigzag or arc structures significantly improve the solidification process, thus optimizing the thermal energy discharge performance. Similarly, innovations in tube arrangements and spacing have decreased PCM melting time and increased heat storage efficiency, as detailed in [15]. These studies suggest that structural modifications in shell-and-tube systems could enhance performance metrics across both charging and discharging phases, thereby addressing some of the core challenges of thermal energy management in LHTES systems. Li et al. [11] developed an axisymmetric two-dimensional and transient model of a shell-and-tube LHTES. The analysis revealed that increasing the specific surface area and porosity led to a steady increase in the PCM's effective usage. However, the investment cost for unit heat storage reached a minimum value. In an exciting development, the study proposed a criterion for distributing cascaded PCMs in the system and confirmed its effectiveness. The optimized model with five cascaded PCMs demonstrated an effective PCM utilization rate of 77.6 %, tripling the performance of a system without cascaded PCMs and reducing costs to approximately 40 % of a non-cascaded system.

Another study shed light on the effect of fin parameters on the energy efficiency of shell-and-tube LHTES systems [16]. Authors found that optimizing fin geometrical parameters and the distribution of cascaded PCMs significantly improved both the melting and solidification times, as well as the overall energy efficiency of the system [16]. Innovative techniques are also being explored to enhance solidification performance. One such approach involved a triplex-tube heat exchanger filled with composite PCM, which led to a notable enhancement in the overall system performance [17]. Furthermore, a study on the melting characteristics of various inner tube designs in double tube latent heat energy storage units revealed a significant improvement in the melting rate with a new elliptical design [18].

Enhancing thermal properties in LHTES systems is vitally important for advancing the field of energy science and engineering [19–22]. A variety of techniques have been identified to achieve this, including the application of extended surfaces [19], porous materials, cascaded or encapsulated PCMs [20,21], nanomaterial additives [20], and innovative geometrical configurations [20]. Particularly, the integration of fins and high-conductivity porous materials such as metal foams is of substantial interest, as they can compensate for the storage material's low thermal conductivity, improving the charging and discharging efficiency of LHTES systems [19]. In addition, nanomaterial additives have been found effective in boosting heat transfer in LHTES systems, consequently improving their storage capabilities [20,23]. Research on nano-enhanced PCMs indicates that certain nanoparticles, like Al_2O_3, copper, and carbon, can greatly boost PCM performance [23]. Encapsulating PCMs has also shown potential for improving thermal conductivity [21]. The composite metal foams are one of the promising approaches for improving heat transfer in LHTES systems. Using a PCM/metal foam composite in a triplex tube heat exchanger can reduce melting times compared to pure PCM. Incorporating varying porosity metal foams and nanoparticles could decrease melting time by up to 83.48 % [24].

Besides, innovations in shell designs and fin configurations have significantly enhanced the performance of Latent Heat Thermal Energy Storage systems, particularly by improving heat transfer rates and reducing the response times of PCMs. Notably, horizontal obround shells have cut PCM melting times by 32 % compared to traditional circular shells, thanks to better heat dynamics enabled by the design [25]. Additionally, the use of sinusoidal wavy fins in multi-tube systems has reduced melting times by up to 38.3 % as more heat transfer fluid tubes are added, highlighting the impact of fin design [26]. Further, adjusting the eccentricity of tubes within these shells has proven crucial, enhancing heat transfer rates significantly and reducing PCM melting times by as much as 76 % [27]. This shows the potential of fine-tuning tube placement and shell design to optimize thermal performance. Moreover, combining expanded graphite and circular fins in these systems not only increases energy storage by 109 % compared to basic PCM setups but also accelerates the discharging process, which is crucial for quick-response applications [28].

LHTES systems have shown promise in large-scale applications and commercialization, but their lower thermal response rate has been a significant challenge. Integrating metal foam (MF) in LHTES systems enhances thermal conductivity, which boosts energy storage and retrieval processes [29,30]. The poor thermal conductivity of PCMs, a limitation of their application in energy storage, can be addressed using high-porosity MFs, leading to more efficient phase change [31]. Research on a PCM-MF composite in an LHTES system using staggered bundled tubes showed this configuration to be highly efficient, offering improved charging/discharging rates [31]. A review highlighted the potential of PCMs and MF in overcoming energy demand-supply mismatch, improving LHTES efficiency [29]. Despite certain inhibitory effects, adding MF can significantly improve phase change heat transfer performance [30].

Most of the literature studies investigated the impact of uniform MFs on the heat transfer enhancement of LHTES systems. However, some recent studies employed non-uniform MFs with porosity gradients or used layers of MFs with different porosities to further enhance the energy storage performance of LHTES systems. The integration of MFs, specifically copper foams, with varying porosity into LHTES systems demonstrates significant potential for thermal performance enhancement [32–35]. Such modification addresses the inherent limitation of PCMs such as paraffin, namely low thermal conductivity, thus expanding their applications [32].

Utilizing copper foams in LHTES revealed a significant improvement in heat transfer performance, reducing full melting time by up to 73.7 % and raising the mean heat rate from 96.38 W to 330.16 W. A particularly effective approach was the division of copper foam into two sections, where porosity increased distinctly along the positive-x and -y directions [32]. Moreover, the combination of MFs with varying porosity and nanoparticles significantly enhances the solidification process in LHTES. Numerical investigations showcased reduced solidification time by 30.15 % as the nanoparticle volume fraction increased from 0 to 0.1. Implementing MFs with uniform porosity led to an 81.2 % reduction in solidification time compared to pure PCM [33]. This model considered differences in thermal conductivity between the PCM and copper foam. Recent research has shown that embedding PCM in heterogeneous metal foams can greatly optimize these systems. By adjusting specific parameters and angles of the foam's heterogeneity, significant heat transfer rate enhancements and melting point reductions are achieved [36]. The study revealed that modifying the heterogeneity parameter and angle can adjust the thermal charging time, with changes of up to 24 % observed when the parameter is adjusted to 0.2, highlighting the capability to customize these elements to boost system performance further [36]. Neural networks were harnessed to optimize the storage unit design, revealing that an anisotropic angle below 45° significantly decreased melting time without compromising thermal energy storage capacity [37]. These findings underscore the significance of tailoring MF configurations, concentration, anisotropic angles, and controlling inlet pressure to enhance the efficiency of LHTES systems.

Investigations on shell-and-tube thermal energy storage units also revealed significant improvements using multiple PCMs and gradient copper foam. While radial multiple PCMs didn't show thermal storage advantages over single PCMs, gradient copper foam configurations demonstrated marked enhancements, with negative gradient configurations showing superior heat transfer effectiveness. A specific negative gradient configuration could result in a 23.7 % decrease in the full melting time [34]. In another study, a porosity gradient increase along the positive y-direction elevated the mean heat transfer rate by 21.6 % in a shell-tube design [35].

While using MFs enhances the thermal response of LHTES systems due to their notable thermal conductivity and high surface-area-to-volume ratio, this incorporation has trade-offs. MFs reduce the thermal capacity and natural convection of LHTES systems. Recently, a shift towards using partial layers of metal foams to fill LHTES systems has been observed in scientific studies, producing noteworthy results. Research presented in [38] utilized a hybrid heat transfer enhancement strategy, combining partial metal foam and nano-additives in an LHTES. The study showed that this combination was more effective than using either enhancement technique separately. In terms of numerical data, the charging power of the LHTES could be improved up to four times compared to the case of pure PCM, with only a minor 3 % reduction in the thermal storage capacity. Ying et al. [39] examined the thermal behavior of LHTES units partially filled with metal foam. They found that the flow rate of liquid paraffin in a bottom-filling configuration was much higher than in a top-filling configuration, facilitating heat transfer enhancement.

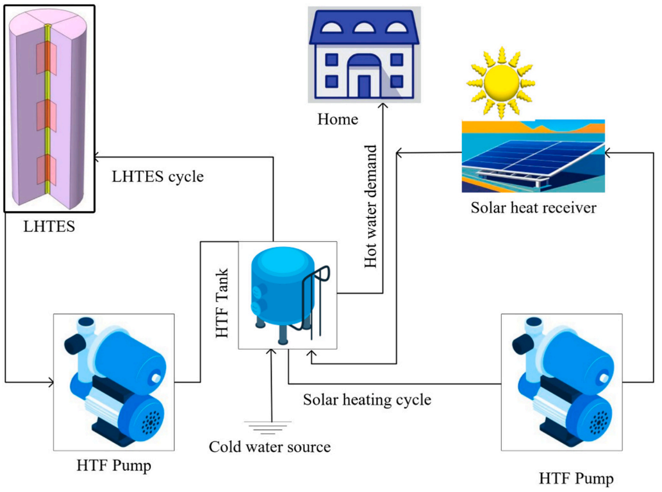

Fig. 1. A representation of a hybrid heating electric solar system with a LHTES unit.

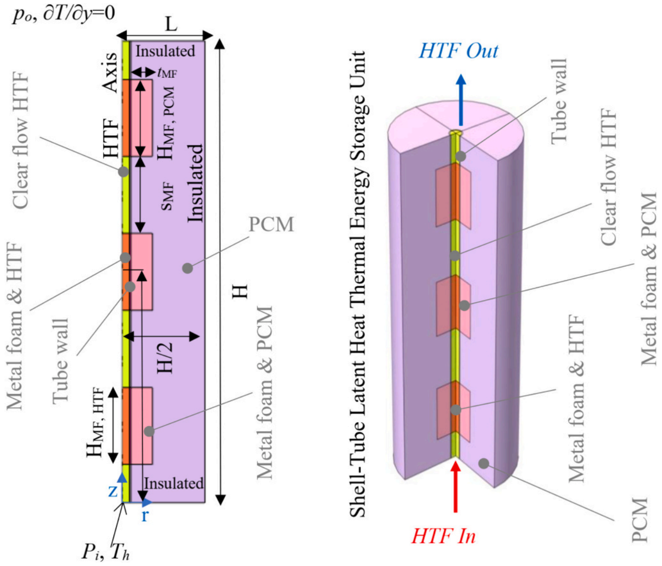

Fig. 2. Schematic view of LHTES unit and physical model. The heat transfer fluid (HTF), phase change material (PCM), metal foam layer (MFL) in the PCM domain, metal foam (MF) inserts in the HTF domain, and tube wall regions are indicated in the figure.

In a different perspective, Yang et al. [40] introduced a strategy of partially filling porous foam in a shell-and-tube unit, which resulted in a 10.5 % energy storage efficiency compared to the same case but fully filled. The authors found an optimal filling ratio of 0.89 for this enhancement. Moreover, Zuo [41] explored various filling angles and thicknesses for sectorial metal foam in a horizontal shell-and-tube LHTES unit. Notably, an increase in the filling angle enhanced the melting rate, but the enhancement rate decreased significantly beyond 150°. Moreover, they designed an optimal case with a ladder shape, which reduced the total melting time by 45.9 % and decreased the amount of metal foam used by 16.8 % compared to the benchmark design. Besides, diverse scenarios featuring varying MF coverage percentages and layer dimensions were explored. Notably, cases exhibiting higher MF concentrations, such as Cases A-C with 50 % MF layers, demonstrated shorter melting times owing to heightened thermal conductivity and reduced thermal resistance on the side of the HTF [42].

As evidenced in several studies [38–45], the use of partial layers of metal foams within LHTES systems significantly enhances heat transfer rates and accelerates thermal response times while preserving the thermal storage capacity. This research develops a mathematical model to analyze the flow and heat transfer dynamics involving working fluid in the insert layers of metal foam, as well as the interaction between the metal foam and phase change material on the shell side of the storage unit. The investigation introduces partial layers of metal foams on both the heat transfer fluid and phase change material sides, aiming to assess the impact of metal foam's geometrical configuration between these two areas on the overall thermal efficiency of the LHTES unit.

2. Physical model

The depiction of a concentrated solar heating system for the purpose of building heating underscores the significance of LHTES in the progression of solar energy technologies. This is essential due to the intermittent nature of solar energy, which depends on weather conditions and time. LHTES provides the capability to store substantial amounts of energy at fusion temperatures in a limited area, thus alleviating the fluctuations in energy encountered in transitional solar energy systems. The system's composition includes a solar collector, a storage tank, an LHTES unit, and circulation pumps. The collector warms up water, which is then stored as sensible heat in the hot water tank to supply the building with hot water as necessary. Furthermore, an auxiliary cycle links the hot water storage tank with the LHTES unit. During periods of low energy demand or high energy production, the pump within the auxiliary energy storage loop activates, channeling surplus heat to the LHTES unit. On the other hand, when solar energy generation is inadequate, the tank draws energy from the LHTES unit. Fig. 1 presents a diagram of this system.

Fig. 2 presents the design of a LHTES device in a shell-tube shape. The device is made of the shell and HTF tube, which are axis-symmetric; thus, Fig. 2 shows a symmetric plan of the system. Water, serving as the heat transfer fluid, enters the tubing with an initial pressure of P_i and departs from the upper outlet at atmospheric pressure. The tube itself possesses a wall thickness t_{tube} and an outer radius R, and is fabricated from copper. Within the tube, a segment of the shell passage is equipped with a layer of copper-infused metal foam. The space between the tube and shell is filled with paraffin wax PCM. Metal foam layers are attached to the tube and extend into the PCM region to enhance heat transfer further. The MF layers inserted in the PCM region are aligned with the MF inserts inside the tube, although their heights can differ. The number of MF layers in the PCM domain is determined by the fill ratio parameter $VFL = V_{MF}/V_{PCM}$, representing the volume of the MF layer compared to the total volume of the PCM region. For instance, $VFL = 0.3$ indicates that 30 % of the PCM enclosure is filled with MF. Thus, the geometry of the MF inserts shown in Fig. 2 can be controlled by adjusting the thickness and height of the MF. The MF height, H_{MF}, is considered an independent parameter that will be investigated in the current research. To maintain a constant VFL parameter, the thickness of the MF layer is determined as a function of VFL, ensuring that the volume of PCM remains unchanged.

During its phase transition, the PCM stores or releases latent heat at a temperature T_f. Based on whether the system is in a charging or discharging phase, water conducts heat through the tube wall to the paraffin wax PCM region, altering its exit temperature either upward or downward. To accommodate the capacity and demand specifications of the cycle shown in Fig. 1, multiple LHTES units can be arranged in parallel, series, or a hybrid of both configurations. The primary aim is to examine the heat transfer design within the LHTES unit, which features a layer of heterogeneous foam.

The heat transfer dynamics within the unit are divided into two main areas: the PCM storage unit and the heat transfer fluid (HTF) side. To increase the rate of heat transfer and decrease the time required for storage, a layer of isotropic metal foam has been integrated into the HTF tube. The foam fills the RRM_{MF} fraction of the tube and can be incorporated in various configurations, as shown in Fig. 2. An $RRM_{MF} = 0.50$

Table 1
The operating conditions and geometrical details of the model.

Model parameter	Default value
Geometrical specifications	
Inner tube radius	0.527/2 in (6.7 mm)
Tube thickness	0.049 in (1.245 mm)
Tube nominal radius	1/4 in (6.35 mm)
L	6× Tube nominal radius (38.1 mm)
H	400 mm
Shell Volume	1.745 Liter
$H_{\mathrm{MF,HTF}}$	$H/6$
$H_{MF,PCM}$	$HLR \times H_{\mathrm{MF,HTF}}$
Volume of MF in Shell	Shell Volume×RRV_{MF}
t_{MF}	From Eq. (1)
S_{MF}	$H_{\mathrm{MF,HTF}}/2$
Model parameters	
A_{mush}	10^{10} Pa.s/m^2
E_s	0.001
ε	0.95
ω	40 PPI
Operating specifications	
Gravity acceleration (g)	9.81 m/s^2
Reference temperature	T_f (K) -15
Initial temperature (Tc)	T_f (K) -15
Inlet temperature (T_{in})	T_f (K) +15
Inlet pressure (P_i)	Model variable (750 Pa)

was adopted in the present study. When the temperature of the LHTES unit is initially low ($Tc < Th$), the hot tank at a steady high temperature (Th) transfers surplus energy to the LHTES unit. Therefore, Th is considered as the intake temperature for the HTF during the charging process. The operation temperature and specifications are reported in Table 1, while the LHTES unit thermophysical properties are listed in Table 2.

The cycle diagram provides an overview of the application. The important design parameters are the pressure difference and the heat transfer rate (power) across the LHTES unit, which are addressed in the present study. The pressure difference dictates the required pumping power, while the energy storage power defines the amount of energy transferred to the HTF fluid flowing inside the LHTES.

In this research, the metal foam layer (MFL) volume was held constant (V_{MF}) for each investigation, with the layer height serving as the adjustable parameter. The layer width depends on the initial MF volume and the chosen layer height. Therefore, the following relationship was employed to calculate the thickness of the MFL.

$$t_{MF} = \sqrt{\frac{\textit{Volume of MF in Shell}}{3\pi H_{MF,PCM}} + (\text{Inner tube radius} + \text{Tube thickness})^2} - (\text{Inner tube radius} + \text{Tube thickness}) \tag{1}$$

Since the volume of the shell is fixed, the control parameter for the amount of MFL volume is adopted as $RRV_{\mathrm{MF}} = V_{\mathrm{MF}}/(\text{Shell Volume})$. Thus, RRV_{MF} can be varied in range 0–1. The height of the MFL was also scaled compared to the heights of the MF insert in the HTF domain as: $FL = H_{\mathrm{MF,PCM}}/H_{\mathrm{MF,HTF}}$. The height ratio parameter (FL) can be changed in the range of 0.75 to 1.75, where for a height ratio below/higher than the unit, the height of MFL is shorter/taller than the height of the MF insert. Fig. 3 shows the impact of FL on the shape of MF in the PCM domain. Since the amount of MF in the PCM domain was considered fixed as $VFL = 0.3$, the variation of FL changes the thickness and height of the MF, as explained in Eq. (1).

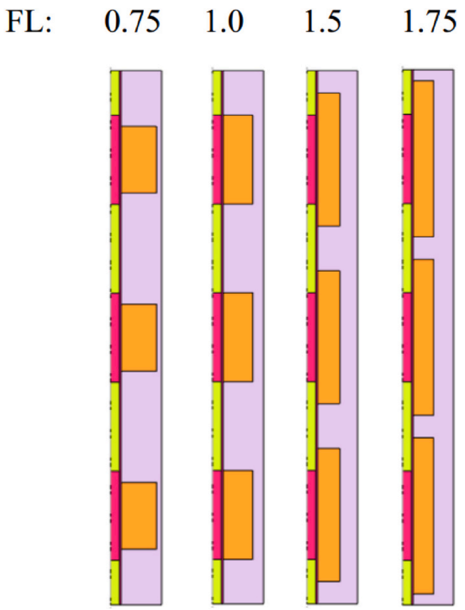

Fig. 3. Impact of FL on the geometrical variation of MF shapes for some selected values of FL.

2.1. Principal equations

This study encompasses various physical domains. Laminar flow and forced convection heat transfer occur within the HTF tube. This transitions to local thermal non-equilibrium (LTNE) forced convection heat transfer in the MF insert at the tube's center. On the shell side, phase change free convection heat transfer occurs in both clear and MFL domains. The heat transfer in the MFL is governed by the LTNE model, which accounts for a temperature field within the pores filled with PCM and another for the solid MFL. There is also a conjugate conduction heat transfer in the tube wall. The governing equations for each domain are laid out in Table 3 [37,42], while Table 4 summarizes the associated closure models. The phase transition occurs within a narrow temperature range to maintain continuity in the energy and hydrodynamic equations. This phase transition is incorporated into the analysis

Table 2
Thermophysical properties of HTF tube, MF, and PCMs.

Materials	k (W/m.K)	ρ (kg/m^3)	C_p (J/kg.K)	μ (kg/m.s)	β (1/K)	L (kJ/kg)	T_f (K)
Paraffin (solid/liquid) [46–48]	0.21/0.12	916/790	2700/2900	0.0036	0.00091	176	322–327
Copper foam [49]	380	8900	386	–	–	–	–
Water [50]	0.613	997.1	4179	0.000957	0.00021	–	–

Table 3
Model's governing equations at each domain.

Domain	Description	Mathematical equation	No.
HTF - Clear region	Continuity	$\left[\frac{\partial u_z}{\partial z}+\frac{1}{r}\frac{\partial(ru_r)}{\partial r}\right]=0$	(2)
	r-Momentum	$\rho_{\mathrm{HTF}}\left(\frac{\partial u_r}{\partial t}+\left[u_z\frac{\partial u_r}{\partial z}+u_r\frac{\partial u_r}{\partial r}\right]\right)=-\frac{\partial p}{\partial r}+\left[\frac{\mu_{\mathrm{HTF}}}{r}\frac{\partial}{\partial r}\left(r\frac{\partial u_r}{\partial r}\right)+\mu_{\mathrm{HTF}}\frac{\partial^2 u_r}{\partial z^2}\right]-\frac{\mu_{\mathrm{HTF}}u_r}{r^2}$	(3)
	z-Momentum	$\rho_{\mathrm{HTF}}\left(\frac{\partial u_z}{\partial t}+\left[u_z\frac{\partial u_z}{\partial z}+u_r\frac{\partial u_z}{\partial r}\right]\right)=-\frac{\partial p}{\partial z}+\left[\frac{\mu_{\mathrm{HTF}}}{r}\frac{\partial}{\partial r}\left(r\frac{\partial u_z}{\partial r}\right)+\mu_{\mathrm{HTF}}\frac{\partial^2 u_z}{\partial z^2}\right]$	(4)
	Energy	$(\rho C_p)_{\mathrm{HTF}}\left(\frac{\partial T}{\partial t}+\left[u_z\frac{\partial T}{\partial z}+u_r\frac{\partial T}{\partial r}\right]\right)=k_{\mathrm{HTF}}\left[\frac{1}{r}\frac{\partial}{\partial r}\left(r\frac{\partial T}{\partial r}\right)+\frac{\partial^2 T}{\partial z^2}\right]$	(5)
HTF - MF region	Continuity	$\left[\frac{\partial u_z}{\partial z}+\frac{1}{r}\frac{\partial(ru_r)}{\partial r}\right]=0$	(6)
	r-Momentum	$\frac{\rho_{\mathrm{HTF}}}{\varepsilon}\frac{\partial u_r}{\partial t}+\frac{\rho_{\mathrm{HTF}}}{\varepsilon^2}\left[u_z\frac{\partial u_r}{\partial z}+u_r\frac{\partial u_r}{\partial r}\right]=-\frac{\partial p}{\partial r}+\frac{\mu_{\mathrm{HTF}}}{\varepsilon}\left[\frac{1}{r}\frac{\partial}{\partial r}\left(r\frac{\partial u_r}{\partial r}\right)-\frac{u_r}{r^2}+\frac{\partial^2 u_r}{\partial z^2}\right]-\rho_{\mathrm{HTF}}\left(\frac{C_F}{\sqrt{\kappa}}\right)\lvert u\rvert u_r-\left(\frac{\mu_{\mathrm{HTF}}}{\kappa}\right)u_r$	(7)
	z-Momentum	$\frac{\rho_{\mathrm{HTF}}}{\varepsilon}\frac{\partial u_z}{\partial t}+\frac{\rho_{\mathrm{HTF}}}{\varepsilon^2}\left[u_z\frac{\partial u_z}{\partial z}+u_r\frac{\partial u_z}{\partial r}\right]=-\frac{\partial p}{\partial z}+\frac{\mu_{\mathrm{HTF}}}{\varepsilon}\left[\frac{\partial^2 u_z}{\partial z^2}+\frac{1}{r}\frac{\partial}{\partial r}\left(r\frac{\partial u_z}{\partial z}\right)\right]-\rho_{\mathrm{HTF}}\left(\frac{C_F}{\sqrt{\kappa}}\right)\lvert u\rvert u_z-\left(\frac{\mu_{\mathrm{HTF}}}{\kappa}\right)u_z$	(8)
	Fluid-Energy	$(\rho C_p)_{\mathrm{HTF}}\left(\varepsilon\frac{\partial T_{\mathrm{HTF}}}{\partial t}+\left[u_z\frac{\partial T_{\mathrm{HTF}}}{\partial z}+u_r\frac{\partial T_{\mathrm{HTF}}}{\partial r}\right]\right)=\left[\frac{1}{r}\frac{\partial}{\partial r}\left(k_{\mathrm{eff,HTF}}r\frac{\partial T_{HTF}}{\partial r}\right)+\frac{\partial}{\partial z}\left(k_{\mathrm{eff},HTF}\frac{\partial T_{HTF}}{\partial z}\right)\right]+h_{sf}A_{sf}(T_{\mathrm{MF}}-T_{\mathrm{HTF}})$	(9)
	MF-Energy	$(\rho C_p)_{\mathrm{MF}}(1-\varepsilon)\frac{\partial T_{\mathrm{MF}}}{\partial t}=\left[\frac{1}{r}\frac{\partial}{\partial r}\left(k_{\mathrm{eff,MF}}r\frac{\partial T_{\mathrm{MF}}}{\partial r}\right)+\frac{\partial}{\partial z}\left(k_{\mathrm{eff,MF}}\frac{\partial T_{\mathrm{MF}}}{\partial z}\right)\right]+h_{sf}A_{sf}(T_{\mathrm{HTF}}-T_{\mathrm{MF}})$	(10)
PCM - Clear region	Continuity	$\left[\frac{1}{r}\frac{\partial(ru_r)}{\partial r}+\frac{\partial u_z}{\partial z}\right]=0$	(11)
	r-Momentum	$\rho_{\mathrm{PCM}}\left(\frac{\partial u_r}{\partial t}+\left[u_z\frac{\partial u_r}{\partial z}+u_r\frac{\partial u_r}{\partial r}\right]\right)=-\frac{\partial p}{\partial r}+A_{mush}\frac{(1-\varphi(T))^2}{\lambda_{mush}+\varphi^3(T)}u_r+\mu_{\mathrm{PCM}}\left[\frac{1}{r}\frac{\partial}{\partial r}\left(r\frac{\partial u_r}{\partial r}\right)-\frac{u_r}{r^2}+\frac{\partial^2 u_r}{\partial z^2}\right]$	(12)
	z-Momentum	$\rho_{\mathrm{PCM}}\left(\frac{\partial u_z}{\partial t}+\left[u_z\frac{\partial u_z}{\partial z}+u_r\frac{\partial u_z}{\partial r}\right]\right)=-\frac{\partial p}{\partial z}+A_{mush}\frac{(1-\varphi(T))^2}{\lambda_{mush}+\varphi^3(T)}u_z+\mu_{\mathrm{PCM}}\left[\frac{\partial^2 u_z}{\partial z^2}+\frac{1}{r}\frac{\partial}{\partial r}\left(r\frac{\partial u_z}{\partial z}\right)\right]+g\rho_{\mathrm{PCM}}\beta_{\mathrm{PCM}}(T-T_0)$	(13)
	Energy	$(\rho C_p)_{\mathrm{PCM}}\left(\frac{\partial T_{\mathrm{PCM}}}{\partial t}+\left[u_z\frac{\partial T_{\mathrm{PCM}}}{\partial z}+u_r\frac{\partial T_{\mathrm{PCM}}}{\partial r}\right]\right)=\left[\frac{1}{r}\frac{\partial}{\partial r}\left(k_{\mathrm{PCM}}r\frac{\partial T_{\mathrm{PCM}}}{\partial r}\right)+\frac{\partial}{\partial z}\left(k_{\mathrm{PCM}}\frac{\partial T_{\mathrm{PCM}}}{\partial z}\right)\right]-\rho_{\mathrm{PCM}}Lf_{\mathrm{PCM}}\frac{\partial\varphi(T)}{\partial t}$	(14)
Tube wall	Energy	$(\rho C_p)_{\mathrm{Wall}}\frac{\partial T}{\partial t}=k_{\mathrm{Wall}}\left[\frac{\partial^2 T}{\partial z^2}+\frac{1}{r}\frac{\partial}{\partial r}\left(r\frac{\partial T}{\partial r}\right)\right]$	(15)
PCM - MFL region	Continuity	$\left[\frac{\partial u_z}{\partial z}+\frac{1}{r}\frac{\partial(ru_r)}{\partial r}\right]=0$	(16)
	r-Momentum	$\frac{\rho_{\mathrm{PCM}}}{\varepsilon}\left(\frac{\partial u_r}{\partial t}+\frac{1}{\varepsilon}\left[u_z\frac{\partial u_r}{\partial z}+u_r\frac{\partial u_r}{\partial r}\right]\right)=-\frac{\partial p}{\partial r}+A_{mush}\frac{(1-\varphi(T))^2}{\lambda_{mush}+\varphi^3(T)}u_r+\frac{\mu_{\mathrm{PCM}}}{\varepsilon}\left[\frac{1}{r}\frac{\partial}{\partial r}\left(r\frac{\partial u_r}{\partial r}\right)-\frac{u_r}{r^2}+\frac{\partial^2 u_r}{\partial z^2}\right]-\rho_{\mathrm{PCM}}\left(\frac{C_F}{\sqrt{\kappa}}\right)\lvert u\rvert u_r-\left(\frac{\mu_{\mathrm{PCM}}}{\kappa}\right)u_r$	(17)
	z-Momentum	$\frac{\rho_{\mathrm{PCM}}}{\varepsilon}\left(\frac{\partial u_z}{\partial t}+\frac{1}{\varepsilon}\left[u_z\frac{\partial u_z}{\partial z}+u_r\frac{\partial u_z}{\partial r}\right]\right)=-\frac{\partial p}{\partial z}+A_{mush}\frac{(1-\varphi(T))^2}{\lambda_{mush}+\varphi^3(T)}u_z+\left(\frac{\mu_{\mathrm{PCM}}}{\varepsilon}\right)\left[\frac{\partial^2 u_z}{\partial z^2}+\frac{1}{r}\frac{\partial}{\partial r}\left(r\frac{\partial u_z}{\partial z}\right)\right]-\rho_{\mathrm{PCM}}\left(\frac{C_F}{\sqrt{\kappa}}\right)\lvert u\rvert u_z-\left(\frac{\mu_{\mathrm{PCM}}}{\kappa}\right)u_z+g\rho_{\mathrm{PCM}}\beta_{\mathrm{PCM}}(T-T_0)$	(18)

(continued on next page)

Table 3 (*continued*)

Domain	Description	Mathematical equation	No.
	Fluid-Energy	$(\rho C_p)_{\mathrm{PCM}}\left(\varepsilon\frac{\partial T_{\mathrm{PCM}}}{\partial t}+\left(u_z\frac{\partial T_{\mathrm{PCM}}}{\partial z}+u_r\frac{\partial T_{\mathrm{PCM}}}{\partial r}\right)\right)=$ $\left[\frac{1}{r}\frac{\partial}{\partial r}\left(k_{\mathrm{eff,PCM}}r\frac{\partial T_{\mathrm{PCM}}}{\partial r}\right)+\frac{\partial}{\partial z}\left(k_{\mathrm{eff,PCM}}\frac{\partial T_{\mathrm{PCM}}}{\partial z}\right)\right]$ $-\varepsilon\rho_{\mathrm{PCM}}Lf_{\mathrm{PCM}}\frac{\partial\varphi(T)}{\partial t}+h_v(T_{\mathrm{MF}}-T_{\mathrm{PCM}})$	(19)
	MF-Energy	$(1-\varepsilon)(\rho C_p)_{\mathrm{MF}}\frac{\partial T_{\mathrm{MF}}}{\partial t}=\left[\frac{1}{r}\frac{\partial}{\partial r}\left(k_{\mathrm{eff,MF}}r\frac{\partial T_{\mathrm{MF}}}{\partial r}\right)+\frac{\partial}{\partial z}\left(k_{\mathrm{eff,MF}}\frac{\partial T_{\mathrm{MF}}}{\partial z}\right)\right]$ $+h_v(T_{\mathrm{PCM}}-T_{\mathrm{MF}})$	(20)
PCM phase field	Liquid field	$\varphi(T)=\begin{cases}0 & T<T_{\mathrm{f}}-\frac{1}{2}\Delta T_{\mathrm{f}}\ \text{(Solidous phase)}\\ \frac{(T-T_{\mathrm{f}})}{\Delta T_{\mathrm{f}}}+\frac{1}{2} & T_{\mathrm{f}}-\frac{1}{2}\Delta T_{\mathrm{f}}\le T\le T_{\mathrm{f}}+\frac{1}{2}\Delta T_{\mathrm{f}}\ \text{(Solidous-Liquid region)}\\ 1 & T>T_{\mathrm{f}}+\frac{1}{2}\Delta T_{\mathrm{f}}\ \text{(Liquid phase)}\end{cases}$	(21)

through the utilization of a phase field parameter φ [51,52]. Within this parameter, a fully liquid region is represented by a value of unity, while a fully solid region is denoted by a value of zero [53]. In the intermediate or "mushy" region where the phase transition occurs, φ undergoes a linear change relative to temperature. A_{mush}, plays a critical role in accurately capturing the flow resistance within the mushy zone of the PCM. Based on recent research [54], the appropriate selection of the mushy zone constant is crucial for stable and accurate simulations. For this study, a value of A_{mush} was carefully selected to balance numerical stability and physical realism, reflecting the permeability characteristics of the metal foam. Given the presence of metal foam regions in the design, a significantly high value of the mushy parameter, denoted as A_{mush}, was selected, set at 10^{10} Pa·s/m^2 [37], to be comparable/higher than the permeability of the metal foam.

Effective thermal conductivity of MF and HTF in the HTF domain [55,56,59,61] can be obtained using:

$$k_{eff}=\frac{1}{(M_A+M_B+M_C+M_D)}\frac{\sqrt{2}}{2}\tag{43}$$

$$M_A=\frac{4\sigma}{((2e^2+\pi\kappa(1-e))k_{MF}+(4-\pi\sigma(1-e)-2e^2)k_{HTF})}\tag{44}$$

$$M_B=\frac{(\varepsilon-2\sigma)^2}{(k_{MF}(e-2\sigma)e^2+k_{HTF}(2e-4\sigma-(e-2\sigma)e^2))}\tag{45}$$

$$M_C=\frac{\left(\sqrt{2}-2\sigma\right)^2}{\left(2\pi\sigma^2\left(1-2\sqrt{2}\,e\right)k_{MF}+2\left(\sqrt{2}-2e-\pi\sigma^2\left(1-2\sqrt{2}\,e\right)\right)k_{HTF}\right)}\tag{46}$$

$$M_D=\frac{2e}{(e^2k_{MF}+(4-e^2)k_{HTF})}\tag{47}$$

$$\sigma=\sqrt{\frac{\sqrt{2}\left(2-\frac{5}{8}\sqrt{2}\,e^3-2\varepsilon\right)}{\left(\pi\left(3-4\sqrt{2}\,e-e\right)\right)}}\tag{48}$$

$$\sigma=\sqrt{\frac{\sqrt{2}\left(2-\frac{5}{8}\sqrt{2}\,e^3-2\varepsilon\right)}{\left(\pi\left(3-4\sqrt{2}\,e-e\right)\right)}},e=0.339\tag{49}$$

For computing $k_{\mathrm{eff,MF}}$ plugs in $k_{\mathrm{HTF}}=0$ and for $k_{\mathrm{eff,HTF}}$ plugs in $k_{\mathrm{MF}}=0$. Moreover, the dynamic μ_{PCM} viscosity of PCM is artificially modified to improve the solver stability and model convergence. The equation $\mu_{\mathrm{PCM}}=\varphi\times\mu_{\mathrm{PCM,l}}+(1-\varphi)\times\mu_{\infty}$ is introduced, where μ_{∞} represents an extraordinarily high viscosity, established at 10^5 Pa.s. This approach guarantees that in the liquid region ($\varphi=1$), the viscosity remains equivalent to the standard dynamic viscosity $\mu_{\mathrm{PCM,l}}$, and it increases significantly in the solid region ($\varphi=0$). The primary purpose of incorporating source terms is to promote zero velocities in solidified zones, and this deliberate increase in dynamic viscosity facilitates this objective. Additionally, this dynamic viscosity specification enhances the solver's stability, simplifies the simulations, and maintains the authenticity of the physical model.

2.2. *Initial and boundary conditions*

Initially, the whole domain is at super cold temperature *Tc*, and then the HTF liquid flows into the tube at a hot temperature *Th* and melts the PCM inside the shell. Thus, the initial condition T = *Tc* was applied. The boundary conditions are the continuity of heat and temperature at the interfaces. For the interfaces of MF (within the LTNE model) and tube wall, the heat flux was divided into two channels. The first channel is the heat coming from the material inside the pores, *i.e.*, $\varepsilon\times q_{\mathrm{PCM}}$ or $\varepsilon\times q_{\mathrm{HTF}}$), which is proportional to the void space. The second channel is heated through the solid matrix, which is proportional to the solid space (1-ε) and can be written as $\varepsilon\times q_{\mathrm{MF}}$. As a result, the interface boundary condition can be written as [37]:

$$q_{\mathrm{Wall}}=\varepsilon q_{\mathrm{PCM}}+(1-\varepsilon)q_{\mathrm{MF}}\tag{50}$$

This approach is critical for accurately capturing the phase change process and preventing numerical issues such as false diffusion, which can distort the interface behavior in phase change modeling, as discussed by Ye and Arıcı [62]. The outflow with zero outlet gauge pressure and inlet pressure of P_i with a uniform temperature of *Th* was applied for the HTF fluid. The impermeability and zero-slip were also applied for all solid surface boundary conditions. A reference pressure point with zero gauge pressure was also applied at the bottom-left corner of the shell [37]. Zero heat flux was also applied to the remaining shell walls.

Table 4
Model equations for computing properties.

Property	Symbol	Equation	No.
Effective thermal conductivity of MF in MFL [55,56]	$k_{\mathrm{eff,MF}}$	$k_{eff,MF} = \frac{(1-\varepsilon)}{3} k_{\mathrm{MF,PCM}}$	(22)
Effective thermal conductivity of PCM in MFL [55,56]	$k_{\mathrm{eff,MF}}$	$k_{\mathrm{eff,PCM}} = k_{\mathrm{PCM}} \frac{\varepsilon + 2}{3}$	(23)
Permeability [55,56]	κ	$\kappa = \frac{\varepsilon^2}{36} \frac{\left(\sqrt{\frac{\kappa_{tor}}{3\varepsilon}} d_{fp}\right)^2}{\kappa_{tor}(\kappa_{tor} - 1)}$	(24)
Pore diameter [57]	d_{fp}	$d_{fp} = 2.54 \times 10^{-2}/PPI$	(25)
Pore characteristics [57]	d_{fs}	$d_{fs} = 1.18 \left\{ \frac{1}{1 - e^{\frac{(\varepsilon - 1)}{0.04}}} \right\} \sqrt{\frac{(1-\varepsilon)}{3\pi}} d_{fp}$	(26)
Pore flow tortuosity [57]	κ_{tor}	$\frac{1}{\kappa_{tor}} = \frac{1}{\varepsilon} \left[\begin{array}{l} \frac{3}{4} + \frac{\sqrt{9 - 8\varepsilon}}{2} \times \\ cos \left\{ \begin{array}{l} \frac{4}{3}\pi + \\ \frac{1}{3} cos^{-1} \left(\frac{8\varepsilon^2 + 27 - 36\varepsilon}{(9 - 8\varepsilon)^{\frac{3}{2}}} \right) \end{array} \right\} \end{array} \right] d_{fp}$	(27)
Forchheimer coefficient [57]	C_F	$C_F = 0.00212 \times \left(\frac{d_{fs}}{d_{fp}}\right)^{-1.63} (1 - \varepsilon)^{-0.132}$	(28)
Volumetric interface heat transfer between PCM and MF in MFL [58]	h_v	$h_v = \frac{k_{\mathrm{PCM}}}{d_{fs}^2} Nu_v$	(29)
Nusselt number in MFL [58]	Nu_v	$Nu_v = \begin{cases} \left(\begin{array}{l} 76.99 - \\ 152.01 \times \varepsilon + 75.04 \times \varepsilon^2 \end{array} \right), & 0 \le Re \le 0.1 \\ \left(\begin{array}{l} 1.72 + 1.71 \times \varepsilon - \\ 3.46 \times \varepsilon^2 \end{array} \right) \times \\ Re^{0.26} \times Pr^{0.28}, & 0.1 < Re \le 1 \end{cases}$	(30)
Nusselt number of HTF in MF insert [43,59]	Nu_{sf}	$Nu_{sf} = \begin{cases} 0.76 Pr^{0.37} Re_{MF}^{0.4}, 1 \le Re_{MF} \le 40 \\ 0.52 Pr^{0.37} Re_{MF}^{0.5}, 40 \le Re_{MF} \le 1000 \\ 0.26 Pr^{0.37} Re_{MF}^{0.6}, 1000 \le Re_{MF} \le 10^5 \end{cases}$	(31)
Interface heat transfer between MF and HTF in MF insert	h_{sf}	$h_{\mathrm{sf}} = Nu_{\mathrm{sf}} \times k_{\mathrm{sf}}/d_{fp}$	(32)
Pore scale Reynolds number in MF insert	Re_{MF}	$Re_{\mathrm{MF}} = \rho_{\mathrm{HTF}} \times d_{sp} \lvert u \rvert/(\varepsilon \times \mu_{\mathrm{HTF}})$	(33)
Pore scale Reynolds number in MFL	Re_{MF}	$Re = d_{fs} \times u_{\mathrm{PCM}} \times \rho_{\mathrm{PCM}}/\mu_{\mathrm{PCM}}$	(34)
Reynolds number in HTF tube	Re	$Re = R \times u_{\mathrm{HTF}} \times \rho_{\mathrm{HTF}}/\mu_{\mathrm{HTF}}$	(35)
Prandtl number in MFL	Pr	$Pr = \mu_{\mathrm{PCM}} \times \rho_{\mathrm{PCM}}/\alpha_{\mathrm{PCM}}$	(36)
Thermal diffusivity in MFL	α_{PCM}	$\alpha_{\mathrm{PCM}} = k_{\mathrm{PCM}}/(\rho C_p)_{\mathrm{PCM}}$	(37)
Thermal diffusivity in MF insert	α_{HTF}	$\alpha_{\mathrm{HTF}} = k_{\mathrm{HTF}}/(\rho C_p)_{\mathrm{HTF}}$	(38)
Prandtl number in MF insert	Pr	$Pr = \mu_{\mathrm{PCM}} \times \rho_{\mathrm{PCM}}/\alpha_{\mathrm{PCM}}$	(39)
Interface surface between MF pore and HTF [43,58–60]	A_{sf}	$A_{sf} = \frac{3\pi \left(1 - e^{-\frac{(1-\varepsilon)}{0.004}}\right) d_{fs}}{0.59 d_{fp}}$	(40)
Heat capacity of PCM	$(\rho C_p)_{\mathrm{PCM}}$	$(\rho C_p)_{\mathrm{PCM}} = \varphi (\rho C_p)_{\mathrm{s}} + (1 - \varphi)(\rho C_p)_{\mathrm{l}}$	(41)
Density of PCM	ρ_{PCM}	$\rho_{\mathrm{PCM}} = \varphi \rho_{\mathrm{s}} + (1 - \varphi)\rho_{\mathrm{l}}$	(42)

Table 5
Relationships for computing the characteristics parameters.

Property	Symbol	Equation	No.
Melting volume fraction	MVF	$MVF = \oint_V \varphi \varepsilon dV / \oint_V \varepsilon dV$	(51)
Stored energy	ES	$ES = ES_{\mathrm{latent}} + ES_{\mathrm{sensible}}$	(52)
Storage power	SP	$SP = ES/t$	(53)
Sensible stored energy	$ES_{sensible}$	$ES_{sensible} =$ $(\rho C_P)_{\mathrm{MF}} (T - T_0) \oint_V (1 - \varepsilon) dV +$ $\left[\oint_V \left(\int_{T_0}^{T} (\rho C_P)_{\mathrm{PCM}} (T) \varepsilon dT \right) dV \right] +$ $(\rho C_P)_{\mathrm{Wall}} V_{\mathrm{Wall}} (T - T_0)$ $+ (\rho C_P)_{\mathrm{HTF}} V_{\mathrm{HTF}} (T - T_0)$	(54)
Latent stored energy	ES_{latent}	$ES_{latent} = \varepsilon \oint_V L_{\mathrm{PCM}} \rho_{\mathrm{PCM}} \varphi dV$	(55)

Table 6
Mesh specifications and computational time.

Mesh parameter	Elements	Computational time
$m = 5$	67,354	20 h 33 min
$m = 6$	78,705	25 h 20 min
$m = 7$	90,087	60 h 23 min
$m = 8$	95,663	47 h 04 min

2.3. *Characteristics parameters*

The melting volume fraction (*MVF*) and stored energy (*ES*), as well as the storage power (*PS*), were considered as the thermal characteristics of the LHTES unit. Moreover, the flow volume rate was also computed as the hydraulic characteristics of the HTF tube. These characteristics were computed according to the relationships provided in Table 5. In the equations presented in Table 5, *V* is the revolved volume, and *dV* is the volume element for computing integral in revolved geometry.

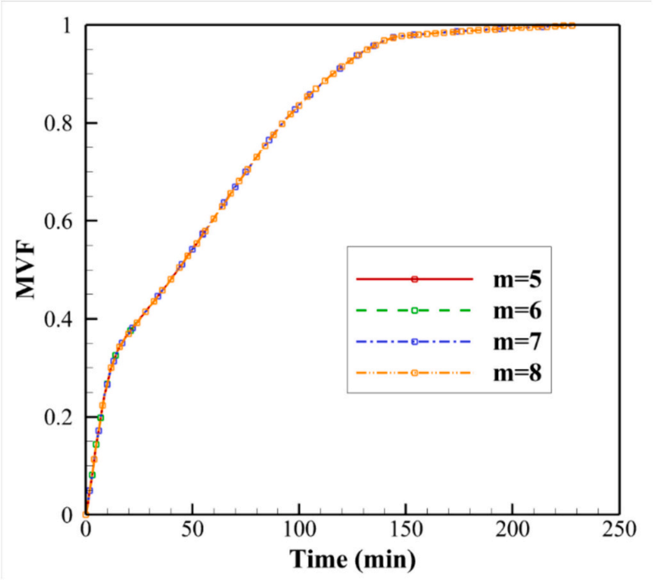

Fig. 4. MVF for four different mesh resolutions.

3. Model simulation and verification

3.1. Solution approach

In this study, the Finite Element Method (FEM) is utilized to solve the partial differential equations outlined in Eqs. (2)–(21), along with the initial and boundary conditions. The momentum and heat transfer equations are transformed into a weak formulation and are addressed using a second-order technique as discussed in reference [63].

This transformation facilitates the equations' integration over elements, a process accomplished *via* Gauss quadrature integration. The product of this is a set of algebraic residual equations, which are subsequently resolved iteratively using the PARDISO solver [64,65]. This solution process incorporates the Newton method, working in a coupled fashion to deliver the solution. To enhance the convergence rate, a damping factor of 0.9 is utilized. The regulation of the time step is achieved by using the backward differential formula (BDF), with a free order that spans between 1 and 2 [66]. This strategy controls the solution's precision while maintaining computational efficiency.

3.2. Mesh examination

A mesh study was conducted to investigate the influence of mesh resolution on the trend and accuracy of numerical simulations. Simulations were run for $P_i = 750$ Pa, $FL = 1.5$, and $RRV_{\mathrm{MF}} = 0.3$, across four different mesh resolutions. The mesh resolution was regulated using a scale parameter, m. Table 6 reports the number of elements and computational time. An increase in the m parameter boosts the number of elements and computational time.

Fig. 4 presents the time history of MVF during the melting process at various mesh resolutions. The results appear to be closely aligned. The model was also simulated with smaller m parameter values and coarse mesh sizes. However, these simulations diverged after approximately 230 s when natural convection effects began. This divergence might be due to the BDF automatic time step control used, maintaining the solution within a relative error of 0.001. The coarse mesh likely could not provide a sufficiently accurate solution for the solver to control. Conversely, the other meshes delivered accurate results, as shown in Fig. 4, since the BDF scheme controlled the solution's accuracy and timestep size.

A mesh with m = 6 was selected for the results section's simulations to balance computational time and solution accuracy. Fig. 5 provides a view of the utilized mesh. Given the mesh's fine detail, a full view appears purely black. Therefore, this figure offers a schematic view of the domain and several zoomed-in sections of the mesh. As observed, a structured non-uniform mesh is present in the HTF domain. The tube wall has a uniform structured mesh. A free quad mesh structure was applied to the PCM and MF domains inside the shell.

3.3. Model validation

To check the accuracy of the model and simulations, the outcomes of the current model are compared with the empirical outcomes of Zheng et al. [49]. The authors conducted a hands-on investigation of paraffin wax melting within a copper metal foam-filled square enclosure. The paraffin, initially at a chilled 14 °C and in solid form, was in an enclosure with dimensions of 100 mm in height and width. An electrical heater, producing a heat flux of 1150 W/m^2, warmed the enclosure's left or the top side. The heat generated was absorbed by the PCM and MF within the enclosure, leading to a gradual increase in the enclosure's

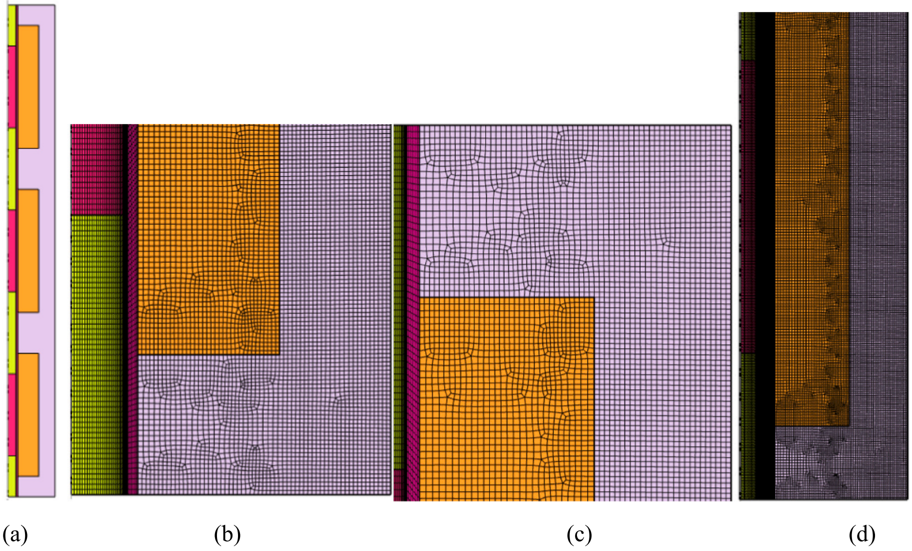
(a) (b) (c) (d)

Fig. 5. Mesh view for the selected Case of $m = 6$: (a) schematic view of the computational domain as a reference, (b) mesh structure at the bottom left of the domain, (c) mesh at the top left, and (c) general view of the mesh at the middle.

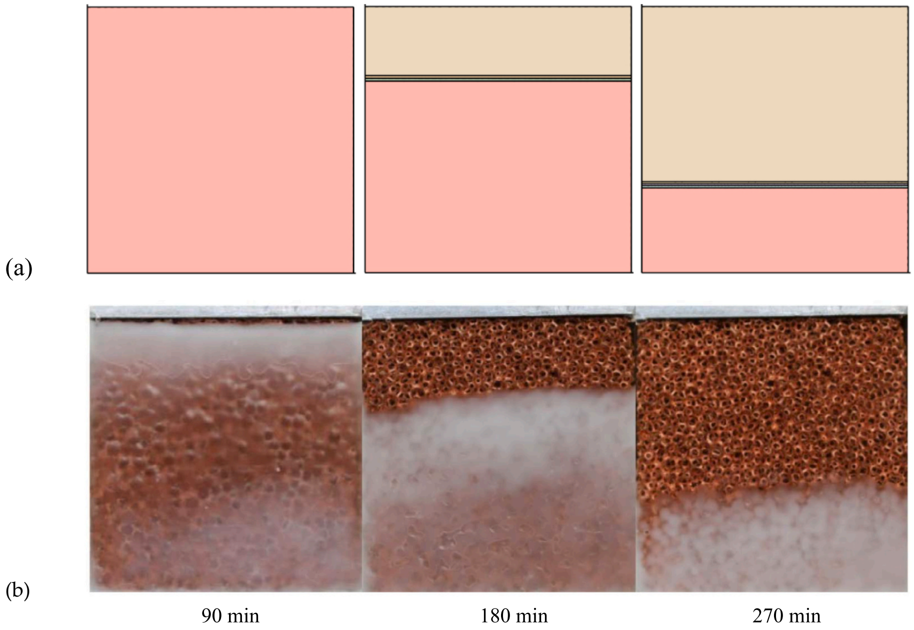

Fig. 6. Verification of the melting heat transfer in an enclosure filled by PCM-MF of porosity 0.95: (a) the present simulations with (b) observations of [49] for the heater at the top.

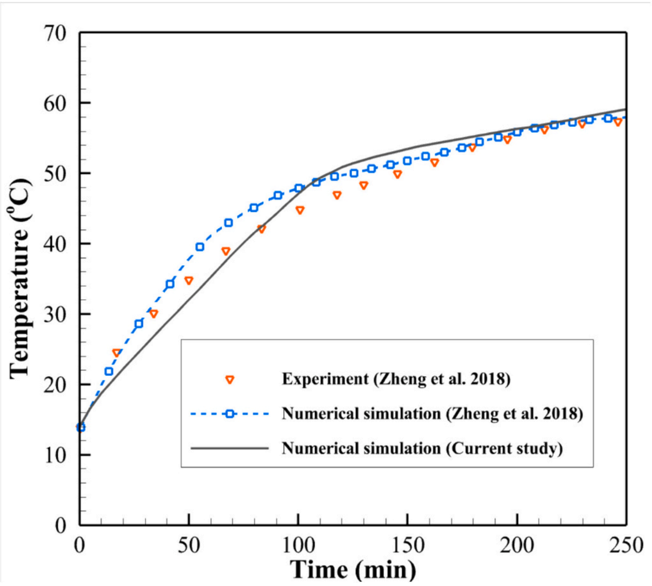

Fig. 7. Heated wall temperature during the melting process reported by [49] against the simulated results of the present research.

temperature until the PCM hit the melting point of 55.3 °C. The porosity was $\varepsilon = 0.95$ with PPI = 5. A comparison of this research's simulation outcomes with Zheng et al. [49] observations are showcased in Fig. 6.

Moreover, the temperature readings were obtained at the heated wall. Fig. 7 draws a comparison between the temporal progression of the measured ([49]) and calculated (current study) temperatures for an enclosure heated from the side and 25 mm from the heated wall. The results of numerical simulations from Zheng et al. [49] have also been reported. The results indicate that the present simulations are in good match with the experimental and numerical data reported in [49].

4. Results and discussions

This comprehensive study offers insightful information regarding the effects of the metal foam layer (FL) shape parameter on thermal energy storage and heat transfer enhancement in an LHTES unit. This analysis studied the operating conditions under three different HTF inlet pressures, $Pi = 250$, 500, and 750 Pa.

The table showcases the impact of varying *FL* parameters and inlet pressures on the heat transfer performance. Here, the Reynolds number (*Re*) - a measure of flow characteristics of the HTF - remains constant for each pressure level. The MVF, indicating the charging state of the LHTES, is also studied at 90 % (MVF = 0.9) and 95 % (MVF = 0.95) levels, and the corresponding time to reach these charging levels and the power at these instances are reported.

A clear trend is noticeable with changes in the *FL* parameter for a given inlet pressure. As the *FL* parameter increases from 0.75 to 1.75, there is a generally decreasing trend in the time required to reach both 90 % and 95 % MVF. This suggests that larger *FL* parameters result in more efficient thermal energy storage, as less time is required to reach a high state of charge. However, this trend has slight deviations, such as for $P_i = 250$ Pa, the time increases when *FL* changes from 1.375 to 1.5.

With the rise in the *FL* parameter, the storage power required to reach these MVF states correspondingly increases. The power required to reach both 90 % and 95 % MVF is generally higher with larger *FL* parameters, implying that while the system reaches a high state of charge more quickly, it does so due to enhanced heat transfer as the fin expands along the heated tube.

Another trend is visible with the increase in inlet pressure. For a given *FL* parameter, a higher inlet pressure results in a reduced time to reach both 90 % and 95 % MVF. It suggests that operating the system at a higher pressure leads to more efficient charging of the LHTES system. Similar to the *FL* parameter, there is an increase in power requirement with the increase in inlet pressure for both MVF states, implying that higher pressure levels provide better storage power.

The study's findings provide some notable peaks and troughs. For instance, the maximum time to reach 90 % MVF (190 min) occurs at the lowest *FL* parameter (0.75) and the lowest inlet pressure (250 Pa). Conversely, the minimum time (115 min) happens at the highest *FL* parameter (1.375) and the highest inlet pressure (750 Pa). These extremes highlight the efficiency gains achievable through optimizing both the *FL* parameter and the inlet pressure. The melting time exhibits a considerable variation of approximately 40 % when altering both the

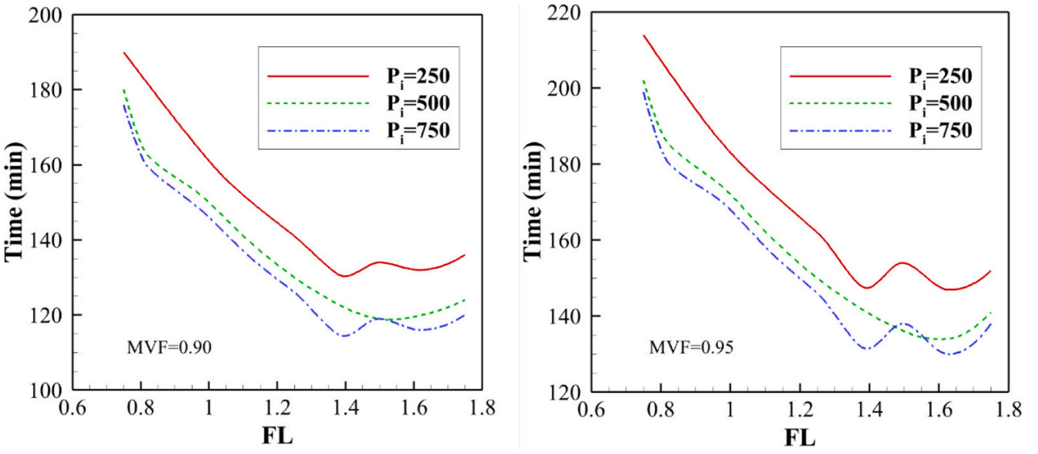

(a)

(b)

Fig. 8. Melting time at various MFL aspect ratios (*FL*): (a) MVF = 0.9, and (b) MVF = 0.95.

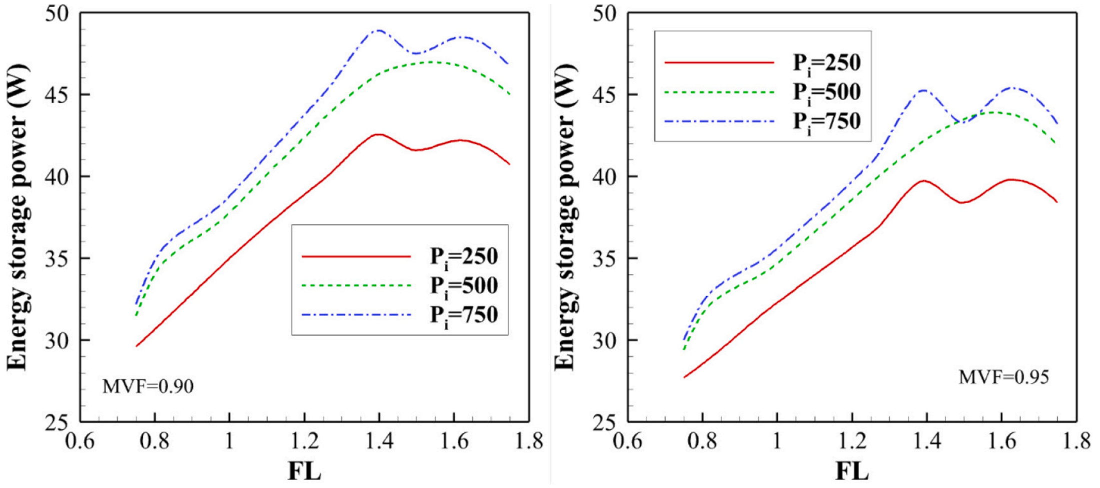

(a)

(b)

Fig. 9. Energy storage power at various MFL aspect ratios (*FL*): (a) MVF = 0.9, and (b) MVF = 0.95.

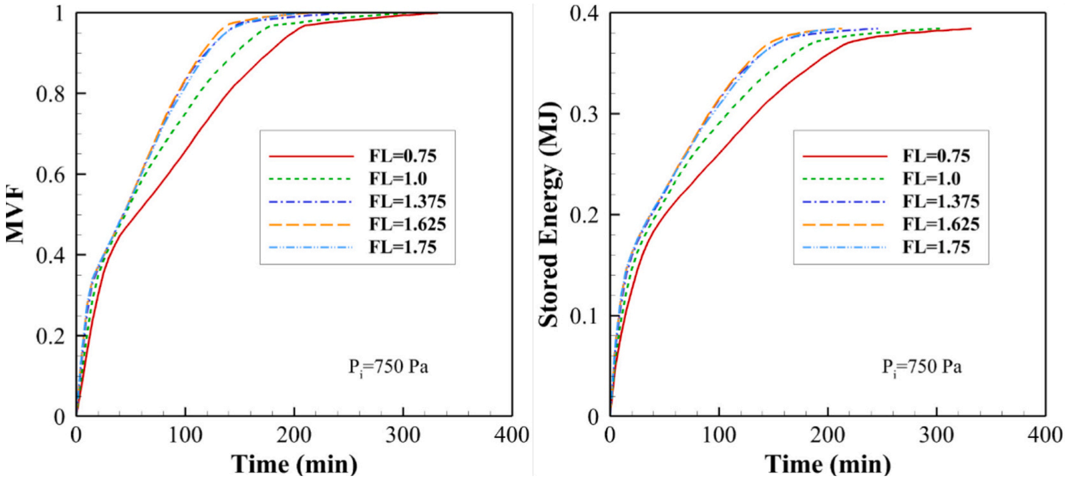

(a)

(b)

Fig. 10. The time-history for the case with the highest inlet pressure (P_i = 750 Pa) and selected cases *FL* = 0.75 (minimum power), *FL* = 1.625, and *FL* = 1.375 (maximum power) for (a) melt fraction, and (b) stored energy.

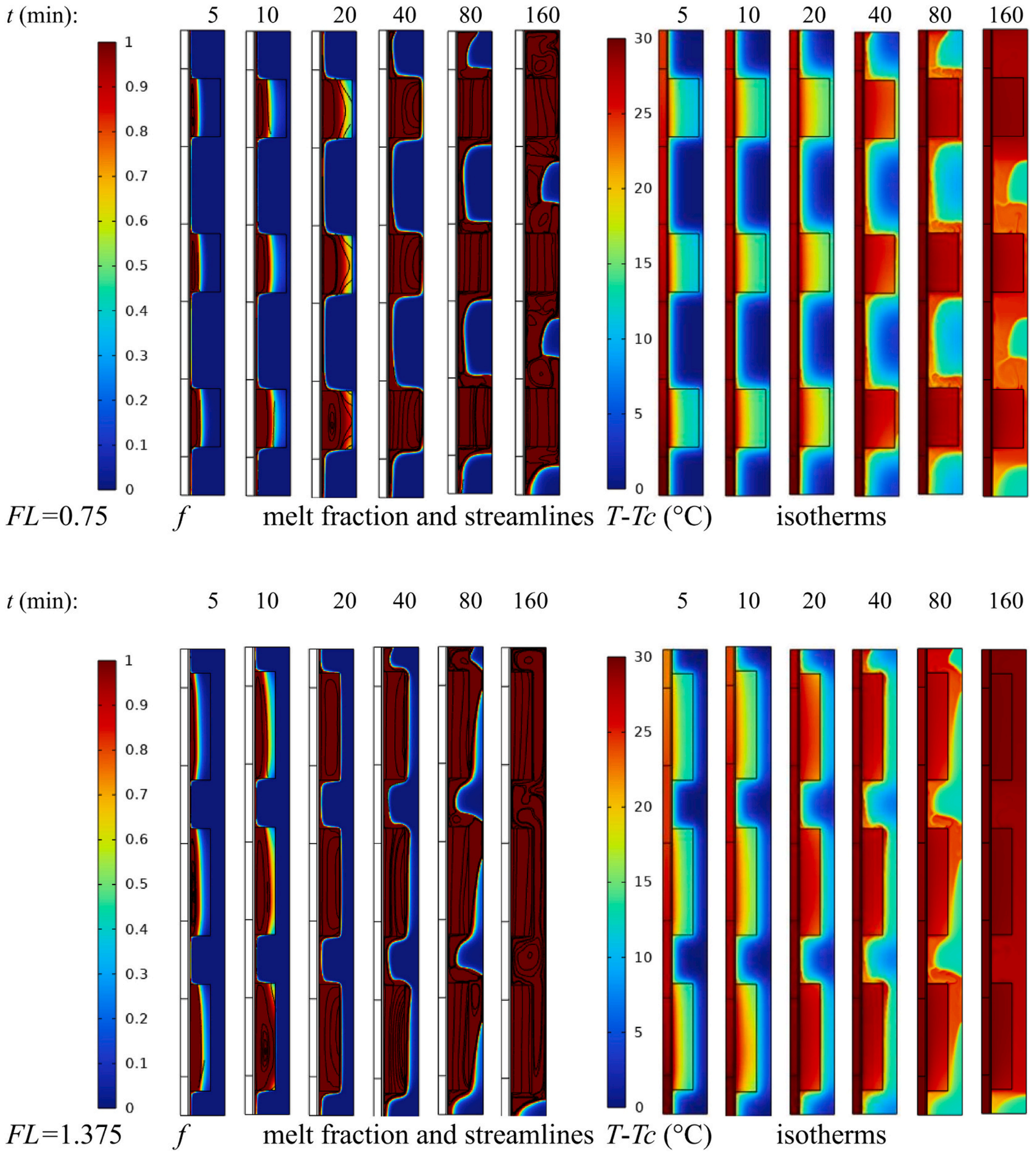

Fig. 11. The melting interface, streamlines, and isotherms when P_i = 750 for two selected cases of *FL* = 0.75 (low charging power) and *FL* = 1.375 (high charging power).

inlet pressure and the MFL (*FL*) shape. Specifically, when maintaining a constant inlet pressure of 750 Pa, the energy storage power for a mean void fraction (MVF) of 0.9 can be modified from 32.2 W at *FL* = 0.75 to 48.7 W at *FL* = 1.37. This significant shift in power output highlights a substantial variation of approximately 34 % achieved solely by adjusting the shape of the MFL.

The results derived from the table are vividly represented in Figs. 8 and 9. Fig. 8 specifically demonstrates the melting time for various *FL* under two distinct conditions - when the MVF is 0.9 and when the MVF is 0.95. Subsequently, Fig. 9 illustrates the energy storage power at these same MFL aspect ratios (*FL*) for two specific situations - with an MVF of 0.9 and when the MVF stands at 0.95.

Fig. 10 provides an in-depth time history for the case bearing the highest inlet pressure, Pi = 750 Pa. This figure presents specific instances of *FL* = 0.75 (indicative of minimum power) alongside *FL* = 1.625 and *FL* = 1.375 (typical of maximum power). It concentrates on two key elements: the melt fraction (see Fig. 10(a)) and the stored energy (refer to Fig. 10(b)). The intricacies of the underlying physics of melting heat transfer are elucidated through the interpretation of the melting interface, streamlines, and isotherms, which are meticulously illustrated in Fig. 11. It focuses on two specific scenarios - when *FL* is 0.75, indicative of low charging power, and when *FL* stands at 1.375, indicating high charging power, both under the condition of $P_i = 750$ Pa.

Analyzing the graphical data represented in Fig. 10(a), one can discern that the scenario with *FL* = 1.375 facilitates a broad MFL over the HTF tube. This condition promptly leads to the melting of the PCM adjacent to the tube within the initial 10 min, and after the 20-min mark, the entirety of the PCM within the MFL is found to be in the molten state. Contrarily, the situation with *FL* = 0.75 only manages to encapsulate a segment of the tube. However, the former case, with FL = 0.75, extends deeper into the PCM domain and similarly melts almost the entire PCM within the MFL domain. Both cases display a somewhat narrow molten region within the clear PCM domain. Therefore, only slight differences are evident in the amount of MVF during the early stages between the two cases.

The case with *FL* = 0.75 presents a marginally lower MVF, attributable to smaller solid regions at the MFL edges deep within the PCM domain. Following this initial phase (t > 80 min), the disparities

Table 7
The investigated cases, melting time and power for 90 % and 95 % melting.

Case	P_i (Pa)	FL	*Re*	MVF = 0.90		MVF = 0.95	
				Time (min)	Power (W)	Time (min)	Power (W)
1	250	0.75	196	190	29.6	214	27.7
2	250	0.825	196	181	31.2	204	29.0
3	250	1.0	196	161	35.0	183	32.3
4	250	1.125	196	150	37.5	172	34.4
5	250	1.25	196	141	39.8	162	36.5
6	250	1.375	196	131	42.4	148	39.6
7	250	1.50	196	134	41.6	154	38.4
8	250	1.625	196	132	42.2	147	39.8
9	250	1.75	196	136	40.7	152	38.4
10	500	0.75	354	180	31.5	202	29.4
11	500	0.825	354	162	34.8	185	32.3
12	500	1.0	354	150	37.8	172	34.7
13	500	1.125	354	139	40.7	160	37.1
14	500	1.25	354	130	43.5	150	39.6
15	500	1.375	354	123	45.9	142	41.9
16	500	1.50	354	119	46.9	136	43.5
17	500	1.625	354	120	46.7	134	43.8
18	500	1.75	354	124	45.0	141	41.9
19	750	0.75	488	176	32.2	199	30.0
20	750	0.825	488	159	35.7	180	33.0
21	750	1.0	488	146	38.8	168	35.6
22	750	1.125	488	135	41.9	156	38.1
23	750	1.25	488	126	45.0	146	40.8
24	750	1.375	488	115	48.7	132	45.1
25	750	1.50	488	119	47.5	138	43.3
26	750	1.625	488	116	48.5	130	45.4
27	750	1.75	488	120	46.7	138	43.2

between MVF, as visible in Fig. 10, become more pronounced, with the scenario at $FL = 0.75$ falling significantly behind the one at $FL = 1.375$. This lag is attributed to the natural convection effects and low conduction resistance between the tube wall and the solid PCM.

In the case of $FL = 1.375$, the MFL is expanded along the tube, providing a low resistance pathway between the residual solid PCM and the tube wall. Conversely, for $FL = 0.75$, only a minor segment of the tube is enhanced by the PCM, and a significant MFL is observed between the tube wall and solid PCM, leading to considerable conduction thermal resistance between solid PCM and the tube wall. Additionally, observing the streamlines reveals that the case with $FL = 1.375$ offers ample space for natural convection in the clear region. In contrast, the extended MFL in case $FL = 0.75$ might partially obstruct natural convection pathways. The temperature contours also affirm efficient conductive heat transfer in MFL for both cases, given that there are minimal temperature gradients within the MFL. However, the temperature gradients are slightly more intense in the case of $FL = 0.75$ due to its thicker MFL shape than the $FL = 1.375$ case. This suggests a slight deviation in heat conduction, marked by the unique shape of the MFL for $FL = 0.75$ compared to that for $FL = 1.375$. This comprehensive analysis aids in understanding the varying dynamics of heat transfer under different conditions and the subsequent influence on the melting process.

A solution was also obtained for the model with no MF insert in the HTF tube as the reference case. In this instance, the inlet pressure was adjusted to achieve a Reynolds number ($Re = 488$) similar to that of case 19 in Table 7. The results indicated a melting time of 240 min (MVF = 0.9) and 265 min (MVF = 0.95). Consequently, the presence of MF inserts in the HTF tube reduced the melting time by 26 % (MVF = 0.9) and 25 % (MVF = 0.95) when compared to the scenario where MF inserts were absent.

5. Conclusions

This study presents an in-depth investigation into the effect of the shape parameter of the metal foam layer and its influence on heat transfer and thermal energy storage efficiency in an LHTES unit. The research focuses on operations under three diverse HTF inlet pressures, $P_i = 250$, 500, and 750 Pa, and the system's melting heat transfer behavior.

A principal finding of the study is the direct correlation between the *FL* parameter and the time necessary for charging the LHTES unit to reach MVF levels of 90 % and 95 %. As the *FL* parameter increases from 0.75 to 1.75, there is a general trend of decreasing time to reach these charging states. Thus, generally an increase of FL improves the melting rate in the LHTES unit. There are only few cases at high values of FL and particularly for low inlet pressure $P_i = 250$ Pa, where the time increased as the *FL* parameter changed from 1.375 to 1.5.

Furthermore, increasing the inlet pressure also enhances the efficiency of the LHTES unit. As the inlet pressure rises, the time required to achieve both 90 % and 95 % MVF is reduced. The energy storage rate was also improved by increasing the inlet pressure.

Significant observations were made regarding the time required to attain certain MVF states. The most prolonged duration to achieve a 90 % MVF (190 min) occurred with the smallest *FL* parameter (0.75) and the lowest inlet pressure (250 Pa). Conversely, the quickest achievement of the same MVF state (115 min) was recorded at the highest *FL* parameter (1.375) and the greatest inlet pressure (750 Pa). Altering the inlet pressure and *FL* could change the melting time by about 40 %.

With a constant inlet pressure of 750 Pa, the energy storage power for MVF = 0.9 (90 % charging) could vary from 32.2 W at $FL = 0.75$ to 48.7 W at $FL = 1.37$. Thus, about 34 % shift in the energy storage rate can be achieved merely by adjusting the MFL shape parameter, *FL*.

CRediT authorship contribution statement

Aeshah Alasmari: Writing – review & editing, Writing – original draft, Methodology, Investigation, Funding acquisition, Formal analysis, Data curation, Conceptualization. **Hakim S. Sultan Aljibori:** Writing – original draft, Investigation, Formal analysis, Conceptualization. **Fathi Alimi:** Writing – original draft, Methodology, Investigation, Formal analysis, Conceptualization. **Mohamed Bouzidi:** Writing – review & editing, Resources, Formal analysis, Data curation, Conceptualization. **Saidul S. Islam:** Writing – original draft, Software, Resources. **Shima Yazdani:** Writing – original draft, Visualization, Validation, Software,

Methodology. **Mohammad Ghalambaz:** Writing – review & editing, Writing – original draft, Supervision, Methodology, Conceptualization.

Declaration of competing interest

The authors clarify that there is no conflict of interest for report.

Data availability

Data will be made available on request.

Acknowledgments

The authors are thankful to the Deanship of Graduate Studies and Scientific Research at University of Bisha for supporting this work through the Fast-Track Research Support Program.

References

[1] Y. Jiang, M. Hajivand, H. Sadeghi, M.B. Gerdroodbary, Z. Li, Influence of trapezoidal lobe strut on fuel mixing and combustion in supersonic combustion chamber, Aerosp. Sci. Technol. 116 (2021) 106841.
[2] S. Ram, A. Prasad, D. Hansdah, A review on solar thermal energy storage systems using phase-change materials, Energy Storage 6 (1) (2024) e541.
[3] W. Liu, Y. Bie, T. Xu, A. Cichon, G. Krolczyk, Z. Li, Heat transfer enhancement of latent heat thermal energy storage in solar heating system: a state-of-the-art review, J. Energy Storage 46 (2022) 103727.
[4] D. Jayathunga, H. Karunathilake, M. Narayana, S. Witharana, Phase change material (PCM) candidates for latent heat thermal energy storage (LHTES) in concentrated solar power (CSP) based thermal applications-a review, Renew. Sust. Energ. Rev. 189 (2024) 113904.
[5] R. Boning, Review on thermal properties and reaction kinetics of ca (OH) 2/CaO thermochemical energy storage materials, Electric. Mater. Appl. 1 (1) (2024) e12007.
[6] Z.H. Low, Z. Qin, F. Duan, A review of fin application for latent heat thermal energy storage enhancement, J. Energy Storage 85 (2024) 111157.
[7] J.J. Gaitero, A. Prabhu, D. Hochstein, R. Mohammadi-Firouz, C. Ouellet-Plamondon, M. Bendouma, D. Snoeck, I. Ramón-Álvarez, S. Sánchez-Delgado, M. Torres-Carrasco, Reviewing experimental studies on sensible thermal energy storage in cementitious composites: report of the RILEM TC 299-TES, Mater. Struct. 57 (4) (2024) 100.
[8] A. Sharma, V.V. Tyagi, C.R. Chen, D. Buddhi, Review on thermal energy storage with phase change materials and applications, Renew. Sust. Energ. Rev. 13 (2) (2009) 318–345.
[9] A. Papadimitratos, S. Sobhansarbandi, V. Pozdin, A. Zakhidov, F. Hassanipour, Evacuated tube solar collectors integrated with phase change materials, Sol. Energy 129 (2016) 10–19.
[10] W.-B. Ye, M. Arıcı, Numerical thermal control design for applicability to a large-scale high-capacity lithium-ion energy storage system subjected to forced cooling, Numer. Heat Transf. Part A: Appl. (2024) 1–15.
[11] M.-J. Li, M.-J. Li, X.-D. Xue, D. Li, Optimization and design criterion of the shell-and-tube thermal energy storage with cascaded PCMs under the constraint of outlet threshold temperature, Renew. Energy 181 (2022) 1371–1385.
[12] W.-B. Ye, M. Arıcı, Redefined interface error, 2D verification and validation for pure solid-gallium phase change modeling by enthalpy-porosity methodology, Int. Commun. Heat Mass Transf. 147 (2023).
[13] W.-B. Ye, M. Arıcı, 3D validation, 2D feasibility, corrected and developed correlations for pure solid-gallium phase change modeling by enthalpy-porosity methodology, Int. Commun. Heat Mass Transf. 144 (2023).
[14] H.S. Sultan, H.I. Mohammed, N. Biswas, H. Togun, R.K. Ibrahem, J.M. Mahdi, W. Yaïci, A. Keshmiri, P. Talebizadehsardari, Revolutionizing latent heat storage: boosting discharge performance with innovative undulated PCM container shapes in vertical shell-and-tube systems, J. Comp. Design Eng. (2024) qwae020.
[15] M.A. Said, K. Hosseinzadeh, A. Bahlekeh, A. Rahbari, M.E. Tiji, J.M. Mahdi, A. Cairns, P. Talebizadehsardari, Accelerated charging dynamics in shell-and-multi-tube latent heat storage systems for building applications, J. Energy Storage 81 (2024) 110286.
[16] G. Czerwiński, J. Wołoszyn, Influence of the longitudinal and tree-shaped fin parameters on the Shell-and-tube LHTES energy efficiency, Energies 16 (1) (2022) 268.
[17] M.T. Alam, A. Raj, L.K. Singh, A.K. Gupta, Configurational assessment of solidification performance in a triplex-tube heat exchanger filled with composite phase change material, Appl. Therm. Eng. 120814 (2023).
[18] M.A. Alnakeeb, W.M. Galal, M.E. Youssef, M.M. Sorour, Melting characteristics of concentric and eccentric inner elliptic tube in double tube latent heat energy storage unit, Alex. Eng. J. 73 (2023) 443–460.
[19] M. Teggar, S.S. Ajarostaghi, Ç. Yıldız, M. Arıcı, K.A. Ismail, H. Niyas, F.A. Lino, M. S. Mert, M. Khalid, Performance enhancement of latent heat storage systems by using extended surfaces and porous materials: a state-of-the-art review, J. Energy Storage 44 (2021) 103340.
[20] R. Elarem, T. Alqahtani, S. Mellouli, F. Askri, A. Edacherian, T. Vineet, I. A. Badruddin, J. Abdelmajid, A comprehensive review of heat transfer intensification methods for latent heat storage units, Energy Storage 3 (1) (2021) e127.
[21] A. Agrawal, D. Rakshit, Review on thermal performance enhancement techniques of latent heat thermal energy storage (LHTES) system for solar and waste heat recovery applications, New Res. Direct. Solar Energy Technol. (2021) 411–438.
[22] Ç. Yıldız, M. Seçilmiş, M. Arıcı, M. Krajčík, A. Shahsavar, W.-B. Ye, H. Karabay, Thermal interaction between water and liquid paraffin wax inside an intertwined enclosure: the role of natural convection in design of latent heat storage units, Therm. Sci. Eng. Progress 47 (2024) 102343.
[23] K. Tofani, S. Tiari, Nano-enhanced phase change materials in latent heat thermal energy storage systems: a review, Energies 14 (13) (2021) 3821.
[24] A. NematpourKeshteli, M. Iasiello, G. Langella, N. Bianco, Enhancing PCMs thermal conductivity: a comparison among porous metal foams, nanoparticles and finned surfaces in triplex tube heat exchangers, Appl. Therm. Eng. 212 (2022) 118623.
[25] N. Parsa, B. Kamkari, H. Abolghasemi, Enhancing thermal performance in shell-and-tube latent heat thermal energy storage units: an experimental and numerical study of shell geometry effects, Int. Commun. Heat Mass Transf. 154 (2024) 107398.
[26] R. Hamid, Z. Mehrdoost, Thermal performance enhancement of multiple tubes latent heat thermal energy storage system using sinusoidal wavy fins and tubes geometry modification, Appl. Therm. Eng. 122750 (2024).
[27] N. Parsa, B. Kamkari, H. Abolghasemi, Experimental study on the influence of shell geometry and tube eccentricity on phase change material melting in shell and tube heat exchangers, Int. J. Heat Mass Transf. 227 (2024) 125571.
[28] A.M. Nair, C. Wilson, B. Kamkari, J. Locke, M.J. Huang, P. Griffiths, N.J. Hewitt, Advancing thermal performance in PCM-based energy storage: a comparative study with fins, expanded graphite, and combined configurations, Energy Convers. Manag. X (2024) 100627.
[29] W. Cui, T. Si, X. Li, X. Li, L. Lu, T. Ma, Q. Wang, Heat transfer enhancement of phase change materials embedded with metal foam for thermal energy storage: a review, Renew. Sust. Energ. Rev. 169 (2022) 112912.
[30] J. Shi, H. Du, Z. Chen, S. Lei, Review of phase change heat transfer enhancement by metal foam, Appl. Therm. Eng. 119427 (2022).
[31] A. Alhusseny, N. Al-Zurfi, A. Nasser, A. Al-Fatlawi, M. Aljanabi, Impact of using a PCM-metal foam composite on charging/discharging process of bundled-tube LHTES units, Int. J. Heat Mass Transf. 150 (2020) 119320.
[32] J. Lei, Y. Tian, D. Zhou, W. Ye, Y. Huang, Y. Zhang, Heat transfer enhancement in latent heat thermal energy storage using copper foams with varying porosity, Sol. Energy 221 (2021) 75–86.
[33] J. Lei, C. Yang, X. Huang, Z. Li, Y. Zhang, Solidification enhancement of phase change materials using nanoparticles and metal foams with nonuniform porosity, J. Energy Storage 44 (2021) 103420.
[34] L. Pu, S. Zhang, L. Xu, Z. Ma, X. Wang, Numerical study on the performance of shell-and-tube thermal energy storage using multiple PCMs and gradient copper foam, Renew. Energy 174 (2021) 573–589.
[35] J. Lei, Y. Huang, C. Yang, X. Xu, Z. Li, Y. Zhang, Numerical study on heat transfer enhancement of shell-and-tube thermal energy storage unit using metal foams with non-uniform porosity, Int. J. Green Energy (2022) 1–14.
[36] M. Ghalambaz, M. Aljaghtham, A.J. Chamkha, A. Abdullah, I. Mansir, M. Ghalambaz, Mathematical modeling of heterogeneous metal foams for phase-change heat transfer enhancement of latent heat thermal energy storage units, Appl. Math. Model. 115 (2023) 398–413.
[37] J. Shafi, M. Ghalambaz, M. Fteiti, M. Ismael, M. Ghalambaz, Computational modeling of latent heat thermal energy storage in a Shell-tube unit: using neural networks and anisotropic metal foam, Mathematics 10 (24) (2022) 4774.
[38] S.M.H. Zadeh, S. Mehryan, M. Ghalambaz, M. Ghodrat, J. Young, A. Chamkha, Hybrid thermal performance enhancement of a circular latent heat storage system by utilizing partially filled copper foam and cu/GO nano-additives, Energy 213 (2020) 118761.
[39] Q. Ying, H. Wang, E. Lichtfouse, Numerical simulation on thermal behavior of partially filled metal foam composite phase change materials, Appl. Therm. Eng. 229 (2023) 120573.
[40] X. Yang, Z. Niu, J. Guo, P. Wei, Y.L. He, Melting evaluation of a thermal energy storage unit with partially filled metal foam, Int. J. Energy Res. 46 (1) (2022) 195–211.
[41] H. Zuo, M. Wu, K. Zeng, Y. Zhou, J. Kong, Y. Qiu, M. Lin, G. Flamant, Numerical investigation and optimal design of partially filled sectorial metal foam configuration in horizontal latent heat storage unit, Energy 237 (2021) 121640.
[42] M. Ghalambaz, M. Sheremet, Z. Raizah, N. Akkurt, M. Ghalambaz, Latent heat thermal energy storage in a shell-tube design: impact of metal foam inserts in the heat transfer fluid side, J. Energy Storage 73 (2023) 108893.
[43] V. Joshi, M.K. Rathod, Thermal transport augmentation in latent heat thermal energy storage system by partially filled metal foam: a novel configuration, J. Energy Storage 22 (2019) 270–282.
[44] V. Joshi, M.K. Rathod, Thermal performance augmentation of metal foam infused phase change material using a partial filling strategy: an evaluation for fill height ratio and porosity, Appl. Energy 253 (2019) 113621.
[45] V. Joshi, M.K. Rathod, Constructal enhancement of thermal transport in metal foam-PCM composite-assisted latent heat thermal energy storage system, Numer. Heat Transf. A Appl. 75 (6) (2019) 413–433.
[46] A.I.N. Korti, H. Guellil, Experimental study of the effect of inclination angle on the paraffin melting process in a square cavity, J. Energy Storage 32 (2020) 101726.

[47] A. Agarwal, R. Sarviya, Characterization of commercial grade paraffin wax as latent heat storage material for solar dryers, Mater. Today Proc. 4 (2) (2017) 779–789.

[48] N. Ukrainczyk, S. Kurajica, J. Šipušić, Thermophysical comparison of five commercial paraffin waxes as latent heat storage materials, Chem. Biochem. Eng. Q. 24 (2) (2010) 129–137.

[49] H. Zheng, C. Wang, Q. Liu, Z. Tian, X. Fan, Thermal performance of copper foam/paraffin composite phase change material, Energy Convers. Manag. 157 (2018) 372–381.

[50] S.-K. Choi, S.-O. Kim, T.-H. Lee, Dohee-Hahn, computation of the natural convection of nanofluid in a square cavity with homogeneous and nonhomogeneous models, Numer. Heat Transf. Part A: Appl. 65 (4) (2014) 287–301.

[51] X. Luo, J. Gu, H. Ma, Y. Xie, A. Li, J. Wang, R. Ding, Numerical study on enhanced melting heat transfer of PCM by the combined fractal fins, J. Energy Storage 45 (2022) 103780.

[52] M. Gürtürk, B. Kok, A new approach in the design of heat transfer fin for melting and solidification of PCM, Int. J. Heat Mass Transf. 153 (2020) 119671.

[53] J. Wołoszyn, K. Szopa, G. Czerwiński, Enhanced heat transfer in a PCM shell-and-tube thermal energy storage system, Appl. Therm. Eng. 196 (2021) 117332.

[54] W.-B. Ye, M. Arıcı, Exploring mushy zone constant in enthalpy-porosity methodology for accurate modeling convection-diffusion solid-liquid phase change of calcium chloride hexahydrate, Int. Commun. Heat Mass Transf. 152 (2024).

[55] S. Zhang, Y. Yao, Y. Jin, Z. Shang, Y. Yan, Heat transfer characteristics of ceramic foam/molten salt composite phase change material (CPCM) for medium-temperature thermal energy storage, Int. J. Heat Mass Transf. 196 (2022) 123262.

[56] Y. Yao, H. Wu, Interfacial heat transfer in metal foam porous media (MFPM) under steady thermal conduction condition and extension of Lemlich foam conductivity theory, Int. J. Heat Mass Transf. 169 (2021) 120974.

[57] Y. Yao, H. Wu, Macroscale modeling of solid–liquid phase change in metal foam/paraffin composite: effects of paraffin density treatment, thermal dispersion, and interstitial heat transfer, J. Therm. Sci. Eng. Appl. 13 (4) (2021).

[58] Y. Yao, H. Wu, Z. Liu, Direct simulation of interstitial heat transfer coefficient between paraffin and high porosity open-cell metal foam, J. Heat Transf. 140 (3) (2018).

[59] X. Yang, P. Wei, X. Wang, Y.-L. He, Gradient design of pore parameters on the melting process in a thermal energy storage unit filled with open-cell metal foam, Appl. Energy 268 (2020) 115019.

[60] V.V. Calmidi, R.L. Mahajan, Forced convection in high porosity metal foams, J. Heat Transf. 122 (3) (2000) 557–565.

[61] Z. Liu, Y. Yao, H. Wu, Numerical modeling for solid–liquid phase change phenomena in porous media: Shell-and-tube type latent heat thermal energy storage, Appl. Energy 112 (2013) 1222–1232.

[62] W.-B. Ye, M. Arıcı, False diffusion, asymmetrical interface, and equilibrious state for pure solid-gallium phase change modeling by enthalpy-porosity methodology, Int. Commun. Heat Mass Transf. 144 (2023).

[63] O.C. Zienkiewicz, R.L. Taylor, P. Nithiarasu, The Finite Element Method for Fluid Dynamics, Seventh Edition ed, Butterworth-Heinemann, Oxford, 2014.

[64] M. Bollhöfer, O. Schenk, R. Janalik, S. Hamm, K. Gullapalli, State-of-the-art sparse direct solvers, in: Parallel Algorithms in Computational Science and Engineering, Springer, 2020, pp. 3–33.

[65] M. Bollhöfer, A. Eftekhari, S. Scheidegger, O. Schenk, Large-scale sparse inverse covariance matrix estimation, SIAM J. Sci. Comput. 41 (1) (2019) A380–A401.

[66] G. Söderlind, L. Wang, Adaptive time-stepping and computational stability, J. Comput. Appl. Math. 185 (2) (2006) 225–243.